CrossMark

Extreme small-scale wind episodes over the Barents Sea: When, where and why?

Erik W. Kolstad

Abstract The Barents Sea is mostly ice-free during winter and therefore prone to severe weather associated with marine cold air outbreaks, such as polar lows. With the increasing marine activity in the region, it is important to study the climatology and variability of episodes with strong winds, as well as to understand their causes. Explosive marine cyclogenesis is usually caused by a combination of several mechanisms: upper-level forcing, stratospheric dry intrusions, latent heat release, surface energy fluxes, low-level baroclinicity. An additional factor that has been linked to extremely strong surface winds, is low static stability in the lower atmosphere, which allows for downward transfer of high-momentum air. Here the most extreme small-scale wind episodes in a high-resolution (5 km) 35-year hindcast were analyzed, and it was found that they were associated with unusually strong low-level baroclinicity and surface heat fluxes. And crucially, the 12 most severe episodes had stronger cold-air advection than 12 slightly less severe cases, suggesting that marine cold air outbreaks are the most important mechanism for extreme winds on small spatial scales over the Barents Sea. Because weather models are often unable to explicitly forecast small-scale developments in data-sparse regions such as the Barents Sea, these results can be used by forecasters as supplements to forecast model data.

1 Introduction

The Barents Sea (see Fig. 1 for a geographical reference) is unique in that it is largely free of sea ice even in the midst of winter. It is a relatively deep shelf sea that receives enormous amounts of heat from the Norwegian Sea (Årthun et al. 2012). Synoptic lows from further south in the North Atlantic do not usually penetrate into the Barents Sea (Hoskins and Hodges 2002; Dacre and Gray 2009; Bader et al. 2011), but the warm ocean surface and the vicinity to the Arctic sea ice makes it vulnerable to marine cold air outbreaks (MCAOs; Kolstad and Bracegirdle 2008), which entail large heat fluxes from the ocean to the atmosphere (Moore et al. 2012). The region is therefore one of the main breeding grounds of polar lows (Rasmussen and Turner 2003) during winter (Kolstad 2006; Zahn and von Storch 2008; Noer et al. 2011).

This is a study of the most severe small-scale wind episodes over the Barents Sea. These matter for many reasons. There is already considerable marine activity in the region. The joint 2013 Norwegian-Russian quota for Barents Sea cod was 1 million tonnes, and the region between Bear Island (Bjørnøya) and the Norwegian coast as well as large regions of the eastern Barents Sea have been opened for petroleum activity. There are thought to be vast reserves of oil and gas in the region (Gautier et al. 2009), and if the Arctic sea ice continues its observed and projected decline (Stroeve et al. 2012), the region may also see a rapid increase in shipping activity along new trade routes from Asia.

Strong winds on small spatial scales in Arctic waters are often inadequately forecast. The scarcity of observational

E. W. Kolstad
StormGeo, Bergen, Norway

Present Address:
E. W. Kolstad (✉)
Uni Research and Bjerknes Centre for Climate Research,
Allégaten 70, 5007 Bergen, Norway
e-mail: erikwkolstad@gmail.com

Fig. 1 The Barents Sea.
Source: Wikimedia Commons

data is an important reason for that, but the spatial resolution of current global forecast model is also too coarse to fully reproduce typical Arctic weather phenomena. A recent polar low case study suggests that it helps to increase the spatial resolution (McInnes et al. 2011). Here the factors (and combinations of factors) that lead to the strongest winds during that period are examined by means of a new high-resolution (5 km), 35-year hindcast based on the European Centre for Medium-Range Weather Forecasts (ECMWF) ERA-Interim reanalysis (Dee et al. 2011).

In recognition of the sometimes poor performance of global models in forecasting extreme winds on small spatial scales, one of the primary objectives of this study is to provide forecasters with simple indicators that can be used when forecast models show a potential for strong winds.

The mechanisms that usually come into play in the development of explosive marine cyclones are, according to Wang and Rogers (2001) (and references therein): (1) strong upper-level forcing, (2) stratospheric dry intrusions, (3) latent heat release, (4) surface energy fluxes, and (5) enhanced local baroclinicity by differential diabetic heating. In addition, Gyakum et al. (1992) have shown that the antecedent spin-up of the low-level disturbance can be an important dynamical pre-conditioning factor. In

reality, a combination of these mechanisms are superposed or work in concert. In the words of Roebber and Schumann (2011): "the strongest maritime storms are in some sense a 'lucky' accident in which the strong baroclinic dynamics of the relative few are preferentially enhanced through feedbacks with the available moisture (such as with moist frontogenesis)."

There is also much to learn from the literature on extreme wind speeds in marine cyclones. The very strongest wind speeds have been referred to as "poisonous tails" (Grønås 1995) and "sting jets" (Browning 2004), and these are found at the edge of the bent-back front (Shapiro and Keyser 1990). Schultz and Sienkiewicz (2013) showed that cold-air advection and strong surface heat fluxes in this region can lead to very low static stability, which facilitates downward momentum transfer and the developments of near-surface jets.[1] Low static stability as an important factor for strong surface wind speeds has also been illustrated

---

[1] Schultz and Sienkiewicz (2013) also note that the sting jets tend to occur in regions with Petterssen (1935) frontolysis, which sets up an indirect thermal vertical circulation with downward advection of high-momentum air.

by Baker et al. (2014) in their idealized simulations of sting jets.

Another well-known cause of strong winds on small scales in Arctic waters are polar lows. These are in many cases similar to rapidly developing larger-scale cyclones, but they are distinct in that: they occur poleward of the main polar front; their spatial scale is sub-synoptic; and they form in association with MCAOs. Many of them develop in reverse-shear conditions (Duncan 1978), with warm air to the east (thermal wind from the south) and flow from the north. In typical extratropical baroclinic developments, the thermal wind and the actual winds are both westerly, and then the thermal wind equation dictates that the wind speed increases with height. But in reverse-shear conditions, the wind speed must decrease with height; in other words, the strongest wind speeds are found at low levels (Kolstad 2006). Note that near the centre of warm core lows, reversed shear is common since the thermal wind is anti-cyclonic.

There exist few studies of strong winds in the Barents Sea region. Kolstad (2008) used indirect satellite-derived wind observations to show that the western part of the region was windier than the eastern part, except for what was subsequently shown by Moore (2013) to be a bora along the east coast of Novaya Zemlya. The Spitsbergen south cape tip jet was identified as the most prominent high-wind feature, and has been studied by Reeve and Kolstad (2011).

A few case studies of polar lows in the Barents Sea region also exist. Rasmussen (1985) found that one polar low near Bear Island developed due to the passage of an upper-level trough, strong sea surface temperature (SST) gradients and large energy fluxes from the ocean to the atmosphere. Incidentally, this polar low interacted with other small-scale disturbances to create new polar lows, a phenomenon studied by Renfrew et al. (1997). Another polar low near Bear Island was studied in detail by Nordeng and Rasmussen (1992). Their conclusion was that it was "triggered by an upper level potential vorticity anomaly in a region of strong low level baroclinicity". The main development was found along the bent-back front. A more recent numerical study of a polar low over the eastern Barents Sea by Føre et al. (2012) suggested that it was fuelled first by baroclinic processes and upper-level forcing and thereafter by intense surface heat fluxes. A concise description of the early stages of polar lows is given by Montgomery and Farrell (1992): "a mobile upper trough initiates a rapid low-level spinup due to the enhanced omega response in a conditionally neutral baroclinic atmosphere".

In this article episodes with strong small-scale wind are identified in the new, high-resolution hindcast. After sorting the cases by their maximum wind speed, the differences between the 12 most severe cases and the next 12 cases are
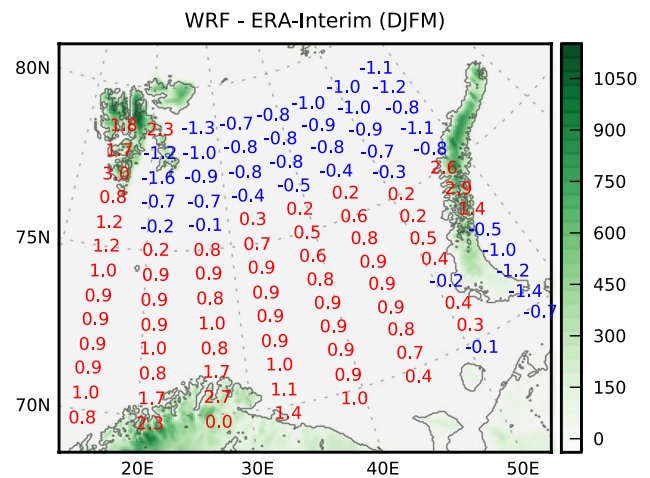

Fig. 2 The geographical extent of the inner 5-km model domain and long-term mean winter (December–March) wind speed differences between the model simulations and ERA-Interim for a selection of points on the ERA-Interim grid

investigated to find out why some storms develop more extreme wind speeds than others. The selection of factors that are studied and quantified was inspired by the studies of explosive marine cyclones and sting jets mentioned earlier.

2 Data and methods

2.1 Model settings

The hindcast covers a period of 35 years (1979–2013). Version 3.5 of the Weather Research and Forecasting (WRF) mesoscale model (Skamarock et al. 2008) was used for all the integrations, which were performed on two nested domains, on horizontal resolutions of 15 km (251 by 181 grid points) and 5 km (337 by 280 grid points). A polar stereographic projection was used. The inner 5 km model domain is shown in Fig. 2, along with the model terrain height. There were 35 vertical levels, with a high density near the surface.

Two-way feedback between the domains was turned on. A cold start strategy was applied, with an individual model run duration of 180 h, of which the first 12 were discarded. The Mellor–Yamada–Janjic (MYJ) planetary boundary layer (PBL) scheme (Janjic 1994) and the corresponding surface layer scheme; the NOAH land surface model (Chen and Dudhia 2001); the MODIS-based land use data; the Thompson microphysics scheme (the new implementation introduced in version 3.1 of WRF) (Thompson et al. 2008); the Kain–Fritsch convection scheme (Kain 2004); and the RRTMG radiation schemes (Iacono et al. 2008) (shortwave and longwave) were used. The WRF algorithm

for adaptive time steps, based on on-the-fly computations of the Courant–Friedrichs–Lewy (CFL) criterion (Courant et al. 1928), was applied.

The ERA-Interim reanalysis was used for initial conditions and on the boundaries. The data had been interpolated to a regular 0.75° by 0.75° grid, and the 60 original model levels were used. The boundary conditions on the outer domain were updated every 3 h, and the analysis time and the sea surface temperatures (SSTs) were updated every 12 h.

2.2 Definitions

In order to investigate the strong wind episodes for the Barents Sea region, an hourly time series (referred to as u_{99} below) was constructed from the spatial 99th percentile (the choice of percentile is discussed later) of the wind speed inside a region between 15°E and 50°E, and between 70.5°N and 76°N. This region was chosen to explicitly exclude orographic features such as the Spitsbergen south cape tip jet and the Novaya Zamlya bora. Dry grid points were ignored.

When evaluating the hindcast, some metrics will be needed. The wind speed 'bias' is:

$$\overline{E} = \overline{u}_m - \overline{u}_o, \tag{1}$$

where $\overline{u}_m$ and $\overline{u}_o$ are the modelled and observed wind speeds, respectively, and the overbars denote temporal means. The ratio of standard deviations (modelled divided by observed) is:

$$\widehat{\sigma}_m = \sigma_m / \sigma_o, \tag{2}$$

where σ_m and σ_o are the standard deviations of u_m and u_o. The differences between the i-th percentiles p_i of the modelled and observed wind speeds are given by:

$$\delta p_i = p_i(u_m) - p_i(u_o). \tag{3}$$

Following Lindzen and Farrell (1980) and Hoskins and Valdes (1990), the Eady growth rate at about 850 hPa is:

$$\sigma = 0.31 \frac{f}{N} \left| \frac{\Delta \boldsymbol{v}}{\Delta z} \right|, \tag{4}$$

where the levels at 925, 850 and 700 hPa were used, f is the Coriolis parameter, N is the buoyancy frequency, and the last factor is the absolute value of the vertical wind shear.

A simple MCAO index was computed as:

$$M = \theta_s - \theta_{700}, \tag{5}$$

where θ_{700} is the potential temperature at 700 hPa and θ_s is the potential SST as given by:

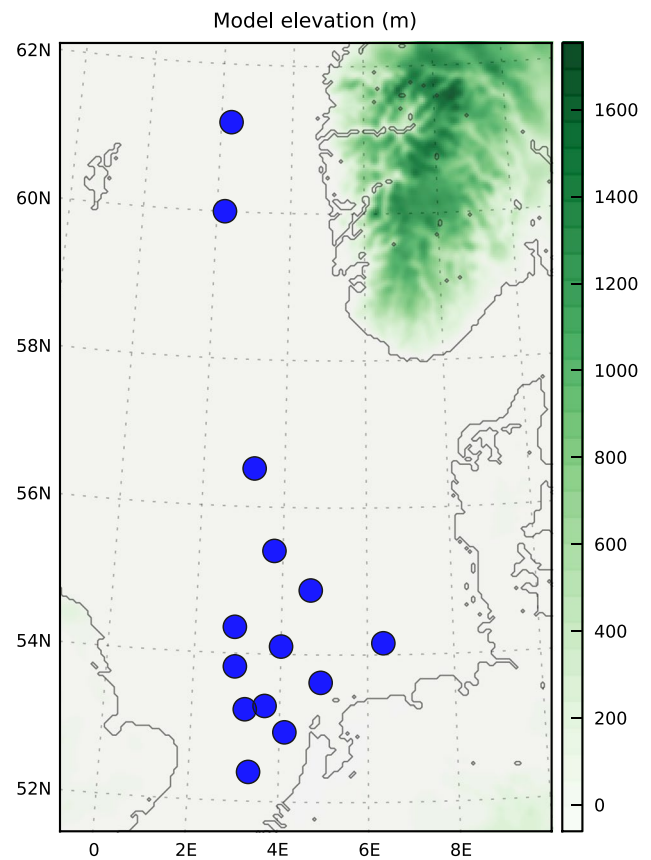$$\theta_s = T_s \left(\frac{p_o}{p_s} \right)^{R/c_p},$$

Fig. 3 The boundaries and terrain height of the inner domain of the model that was used for validation against observations. The *blue dots* show the offshore stations inside the region

where T_s is the SST, p_o is 1,000 hPa, p_s is the pressure at the sea level, R is the gas constant for dry air, and c_p is the specific heat of dry air. When M is high, the static stability is low. Variants of this index have been shown to be reliable indicators of cold air outbreaks over relatively warm water (Bracegirdle and Gray 2008; Kolstad and Bracegirdle 2008).

Some variables below are normalized with respect to climatology. This means that the date-wise mean was subtracted and that the anomaly was divided by the date-wise standard deviation.

2.3 Evaluation of the hindcast

Figure 2 shows the long-term mean winter (DJFM) wind speed differences between the WRF simulations and ERA-Interim for a selection of points on the ERA-Interim grid. There is a positive bias of up to 1 ms^{-1} over the open ocean,[2] and a negative bias over regions that are normally

---

[2] It is possible that this is due to WRF resolving smaller-scale features than ERA-Interim, but that is not investigated here.

Table 1 The aggregated empirical metrics as defined in Eqs. 1–3

Season	$\overline{E}$	$\widehat{\sigma}_m$	δp_{10}	δp_{50}	δp_{90}	δp_{99}	δp_{100}
Overall	0.2	0.95	0.5	0.2	0.0	−0.5	−1.0
Winter	0.3	0.93	0.7	0.5	−0.3	−0.5	−1.3
Autumn	0.5	0.94	0.7	0.6	0.3	−0.8	−0.5
Summer	0.2	0.94	0.4	0.3	−0.1	−0.4	−1.1
Spring	−0.2	0.93	0.3	−0.2	−0.4	−0.4	−1.3

The unit is ms^{-1} for all the metrics except for the dimensionless $\widehat{\sigma}_m$

covered by sea ice in winter. In regions with significant topography, such as near the southern tip of Spitsbergen and on Novaya Zemlya, the positive biases are large, probably because the higher horizontal resolution in WRF enables it to resolve orographically forced wind features. The same feature is seen along the coast of northern Norway.

As there are few direct offshore wind observations in the Barents Sea region, it is difficult to assess whether it is the WRF simulations or ERA-Interim that has the most realistic mean wind speeds. There are no operational oil and/or gas platforms in the area, and the official weather stations are all land-based. It would have been possible to validate against QuikSCAT (Hoffman and Leidner 2005) wind speeds, but concerns have been raised about the validity of the right tail of the QuikSCAT wind speed distribution (Kolstad 2008). A shorter hindcast for the North Sea, where there are ample observations offshore, was therefore produced in order to evaluate the accuracy of the stronger wind speeds in the simulations. In all aspects except for the geographical domain, the model setup used in that short hindcast was identical to the one used in the main hindcast.

The offshore stations that were used in the evaluation are shown in Fig. 3, along with the terrain height of the inner domain of the model. All the stations are offshore platforms, and the observed 10-m wind speeds are derived rather than measured directly. There may be sheltering effects at some of the stations, but what we are interested in is whether or not the hindcast is able to reproduce realistic extreme wind speeds. The observations were therefore used directly; no effort was made to quantify the sheltering effects at the platforms.

In Table 1, the metrics that were defined in Eqs. 1–3 are shown. When computing the aggregated metrics for all the sites, the individual metrics for each site were computed first, and then the aggregated indicators were obtained by taking weighted averages according to the number of valid observations for each site.

The overall wind speed bias ($\overline{E}$ in Eq. 1) is positive (0.2 ms^{-1}); i.e. the WRF wind speeds are higher than the observed ones. This can at least partly be attributed to sheltering effects; the observed wind speeds may be slightly lower than the actual wind speeds. The ratio of the standard deviations ($\widehat{\sigma}_m$ in Eq. 2) shows that the variance of the WRF wind speeds is slightly lower than the variance of the observations.[3]

It is more interesting to look at the wind speed distribution in terms of the percentiles (the δp_i in Eq. 3). WRF has a positive bias for the lower percentiles including the median, but the bias is negative for the higher percentiles. This implies that the extreme wind speeds are underestimated by WRF. However, the mean bias for the maximum wind speed (using only a single observation from each station) is not higher than about −1 ms^{-1}, suggesting that the sample space of strong wind speeds is adequately represented by the model.

3 Results

3.1 Climatology

The mean hindcast 10-m wind speed in January is shown in Fig. 4a. It is known from previous climatologies that the western part of the region is windier than the eastern area (e.g., Fig. 2 in Kolstad 2008) because relatively few large-scale cyclones penetrate into the Barents Sea. There is also a pronounced maximum associated with the Spitsbergen south cape tip jet (Reeve and Kolstad 2011).

Figure 4b shows the 95th percentile of the wind speed for January. Over the open ocean, the geographical pattern is similar to the one found for the mean wind speed, but in regions with prominent topography the extreme wind speeds are much higher than the mean wind speeds. For instance, the south-easterly Novaya Zemlya bora (Moore 2013) is captured by the model, and its impact can be traced some distance downstream.

The long-term monthly means of u_{99} are shown in Fig. 5a. The highest wind speeds are found during the sea ice freezing season from October to March/April. The increase from September to October is steep, and could be a result of the sudden boost in baroclinicity associated with the return of the sea ice.

---

[3] It may seem strange that the overall ratio $\widehat{\sigma}_m$ is higher than all the individual ones for the seasons, but this is due to differences in the annual cycles in WRF and the observations.
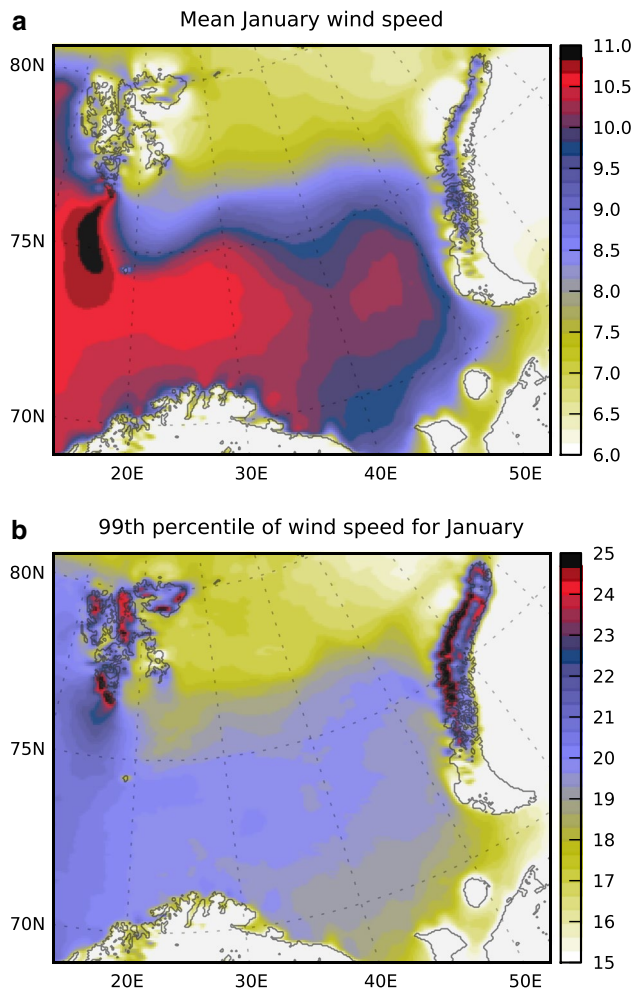
a   Mean January wind speed

b   99th percentile of wind speed for January

Fig. 4 The long-term mean (**a**) and 95th percentile of (**b**) inner-domain hindcast wind speed in January. The unit is ms^{-1}

a   Annual cycle

b   Interannual cycle (Oct-Mar)

Fig. 5 The long-term monthly mean (**a**) and winter mean (**b**: October to March) of u_{99}. The unit is ms^{-1} and the *thick curve* in the *bottom panel* was produced with a LOESS filter

In Fig. 5b, the extended winter (October to March) inter-annual cycle of u_{99} is shown. The thick curves were produced with a simple LOESS (locally weighted scatterplot smoothing) filter (Cleveland and Devlin 1989). For reasons not explored here, the years from 1989 to 1995 were quite windy. This causes a bump to appear in the filtered curve and gives a hint of decadal-scale variability, but the hindcast period is too short for a robust trend analysis.

3.2 Strong wind episodes

Although each individual strong small-scale wind episode is a unique event where several factors may interact non-linearly to yield the strong winds, it is interesting to look for recurring patterns. The most extreme wind events in the study region were selected by objectively identifying maxima in u_{99}, and by requiring that each event was separated from other events by at least 5 days.
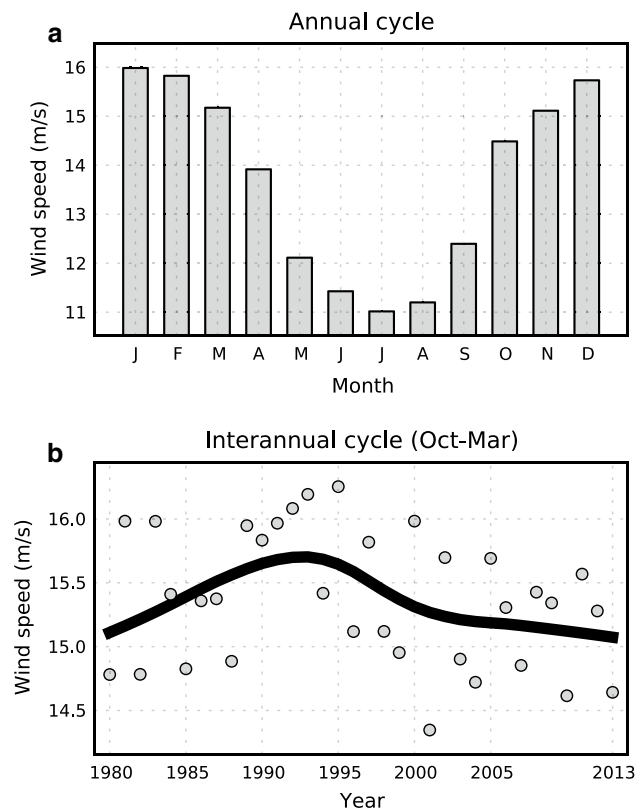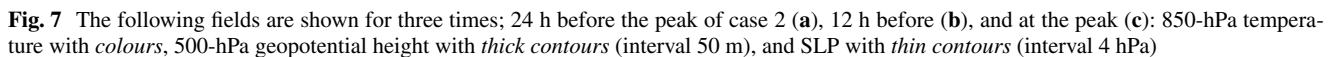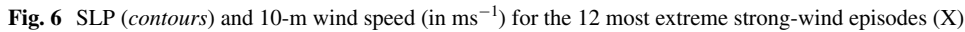
Figure 6 shows snapshots of near-surface wind speed and sea level pressure (SLP) for the 12 most extreme events at their peak intensity. The overall strongest grid-point offshore wind speed in the whole hindcast period occurred during case 2, with a wind speed of 34.3 ms^{-1} 2 h before the time shown in Fig. 6. It will become clear later on that case 2 is typical for this region, so it is now studied in more detail before a composite analysis of strong wind episodes is performed.

3.2.1 A typical case

The synoptic evolution of case 2 is illustrated by the three panels in Fig. 7, which show SLP and the geopotential height at 500 hPa with contours, and the temperature at 850 hPa with colours at the reference time as well as 12 and 24 h before, all for the outer 15 km model domain.

In Fig. 7a (at 1000 UTC on 11 November), a weak surface low centered west of Spitsbergen was moving towards the south-east. The baroclinicity along the warm front was strong due to the contrast between the warm air and the MCAO over the Barents Sea (which was caused by the northerly wind field associated with the upper-level low in

Fig. 6 SLP (*contours*) and 10-m wind speed (in ms^{-1}) for the 12 most extreme strong-wind episodes (X)

Fig. 7 The following fields are shown for three times; 24 h before the peak of case 2 (**a**), 12 h before (**b**), and at the peak (**c**): 850-hPa temperature with *colours*, 500-hPa geopotential height with *thick contours* (interval 50 m), and SLP with *thin contours* (interval 4 hPa)

the right part of the panel). At the same time, a cut-off low at 500 hPa was situated north of the surface disturbance.

In the course of the next 12 h (leading up to Fig. 7b at 2200 UTC on 11 November), the upper-level low spread towards the south over the new MCAO to the west of the surface disturbance. Positive vorticity advection and rising motion above the surface low contributed to its deepening.
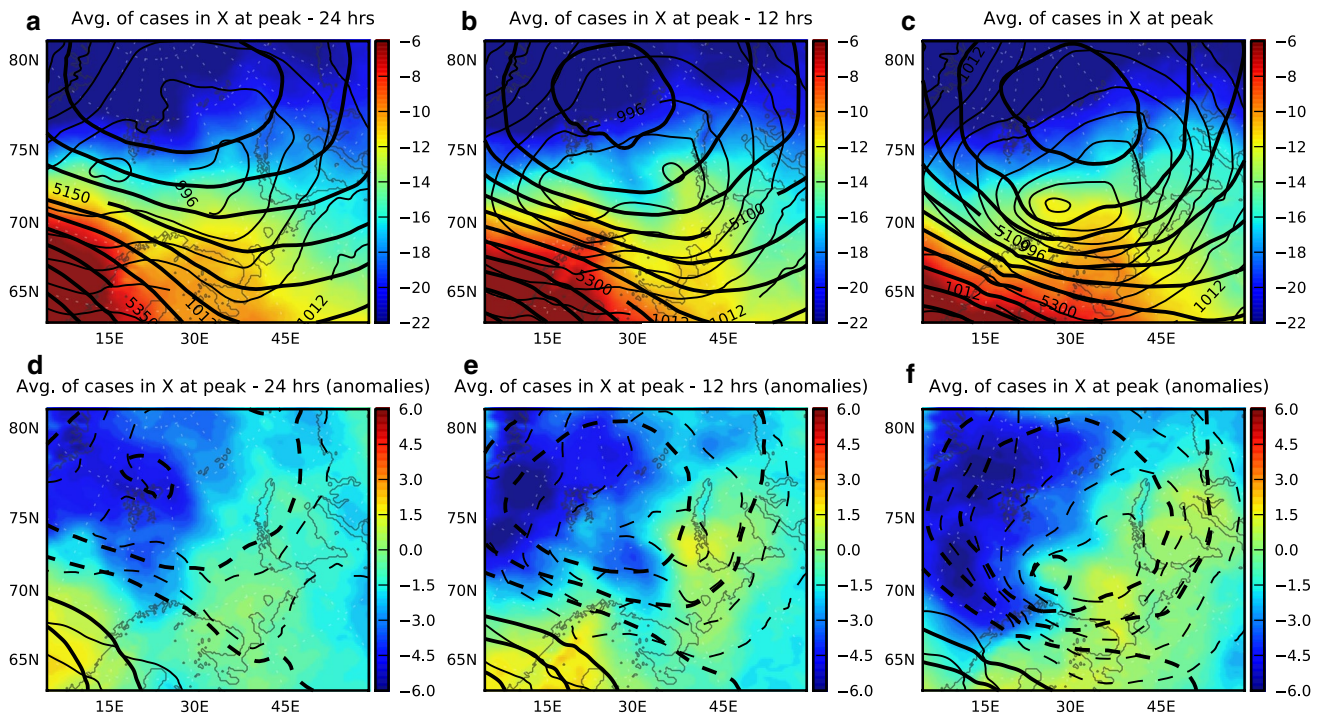
During the 6 h before the time shown in the middle panel, the surface pressure dropped by 9 hPa and the maximum surface wind speed increased by 7 ms^{-1} to 24.5 ms^{-1}. During the next 6 h, the surface pressure dropped by a further 9 hPa and the wind speed increased to 31.4 ms^{-1} at 0400 UTC. The development in this period was strongly baroclinic, and followed the schematic description of baroclinic

Fig. 8 a–c As Fig. 7a–c, but for the average of the 12 cases in X (shown in Fig. 6). **d–f** Anomalies from climatology: 850-hPa temperature with *colours*, SLP with *thin contours* (interval 4 hPa, negative dashed, zero *contour* not shown), and 500-hPa geopotential height with *thick contours* (interval 50 m, otherwise as for SLP)

growth in Fig. 10.27 in Shapiro and Keyser (1990), i.e. deepening of the upper-level trough due to cold advection at lower levels and deepening of the surface low due to positive vorticity advection aloft. The middle panel also shows that the original MCAO had left a pool of cold air near 40°E.

At the peak time (Fig. 7c, at 1000 UTC on 12 November), the upper and lower level lows were in phase, and the polar low was in its mature stage. The surface pressure was no longer decreasing, and the maximum simulated wind speed had occurred 2 h earlier (34.3 ms^{-1} at 0800 UTC). The MCAO to the west of the low was drawing additional strength from the reservoir of cold air that was present near 40°E in the middle panel, and led to simulated surface latent heat fluxes of up to 400 W m^{-2} and sensible heat fluxes of up to 500 W m^{-2}. Note also that the low had a warm core at this stage, suggesting that the region with the strongest winds had reversed shear (and wind speeds decreasing with height) in the region of cold-air advection behind the cold front. The co-location of the strong winds and the vigorous cold-air advection also suggests a possible development of a sting jet.

In summary, case 2 followed a classic baroclinic life cycle, driven by the interaction between a pre-existing surface development and an incoming upper-level trough.

3.2.2 Composite analysis

Not all the cases in Fig. 6 were similar to case 2. The low in case 1 was centred over the north-eastern part of the Barents Sea, the lows in cases 4 and 8 were situated in the south-eastern part, and the low in case 9 had not yet entered the Barents Sea. Nevertheless, the average synoptic evolution across the 12 cases, which is shown in Fig. 8a–c, is rather similar to the one in Fig. 7a–c. The anomalies with respect to climatology are shown in Fig. 8d–f. In order to facilitate the narrative, the composite average will be treated as if it were an actual event.

Figure 8a, d show that 24 h before the peak of the events, there was a warm–cold–warm anomaly wavetrain in the temperature field, with a wavelength of about 40° starting at about 0°. The SLP wavetrain was about a quarter of a wavelength ahead; an ideal environment for growth of baroclinic instabilities (e.g., Holton 2004). During the next 12 h, leading up to the middle panels (Fig. 8b, e), the wavelength decreased and the anomalies grew in magnitude. The cold anomaly around 40°E was important because it represented a reservoir for the MCAO in the next phase, just as seen in case 2. Note also that the 'parent' low to the east of the developing cyclone provided warm air (as seen over Novaya Zemlya in Fig. 8e) that contributed to the formation of a warm core in the next phase.
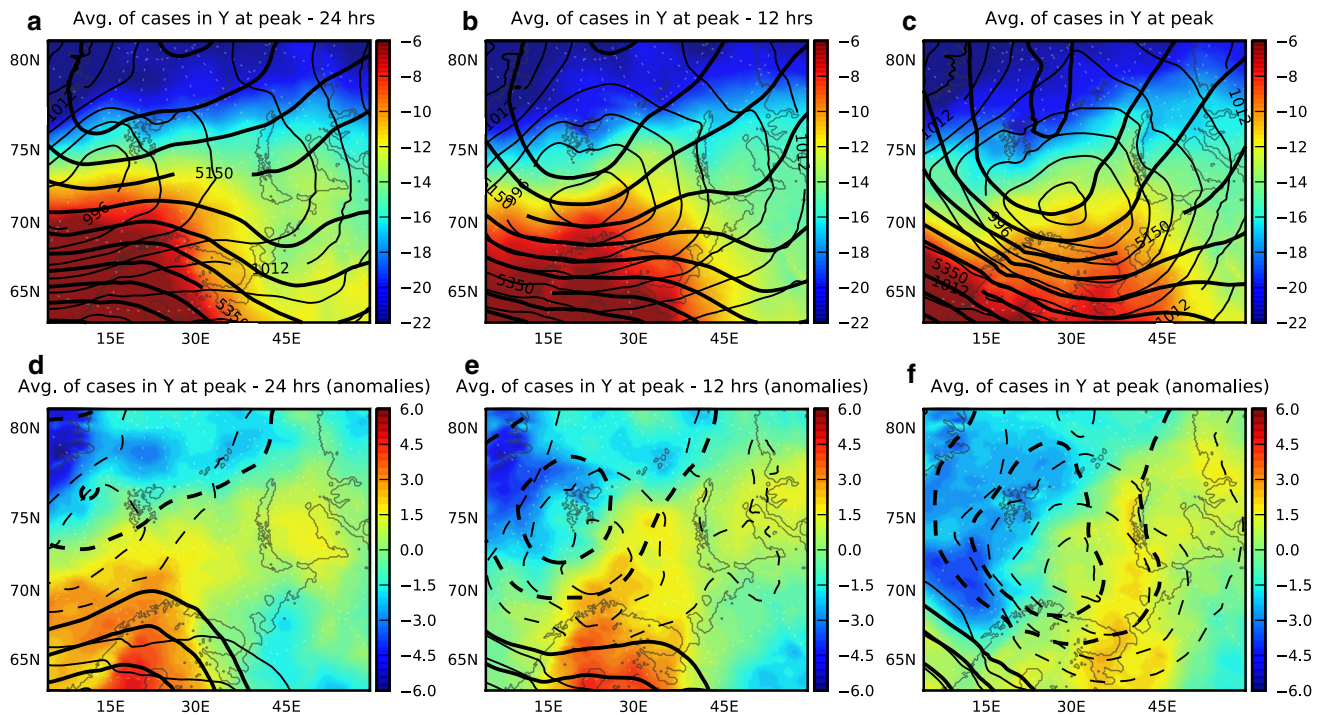
Fig. 9 As Fig. 8, but for the 12 cases in Y

At the peak time (Fig. 8c, f) the lows aloft and near the surface were more or less in phase. There was now a powerful MCAO underway over the western Barents Sea, tapping both from the air masses coming down from the Fram Strait (between Svalbard and Greenland) and from the previously mentioned pool of cold air. There was a warm core, the baroclinicity west of the surface low was high, and the air at 850 hPa was cold (and hence the static stability was low), fuelling further growth or at least contributing to the maintenance of the cyclone. Note also that, as in case 2, the actual winds were antiparallel to the thermal wind, enabling the low-level jet to penetrate down to the surface (reversed shear). And also as in case 2, the strongest winds were found to the south-west of the low.

Having established that the average synoptic evolution of the 12 most extreme strong wind episodes (referred to as the set X from now on) was similar to the actual evolution of case 2, an interesting question arises. What made these particular cases so extreme? Why didn't they just develop as regular, less intense baroclinic cyclones? The answer can be obtained by comparing Fig. 8 to the corresponding fields for the next 12 cases on the list based on u_{99} (i.e. cases 13–24; Y hereafter).

The average evolution of the cases in Y is shown in Fig. 9. Clearly, there was no pre-existing MCAO in the region where the disturbances intensified, such as there was for the cases in X (Fig. 8). The average flow aloft was from the south-west, whereas it was from the north-east for X. An MCAO

did develop eventually, but this was set up the cyclone itself. The cold air was drawn from the Fram Strait region, but the pre-existing pool of cold air that probably fuelled the developments of the cases in X did not exist for the cases in Y.

The differences between the anomalies for X and Y are shown in Fig. 10 and confirm that the cyclones in X developed in more northerly flow and in much colder air than the ones in Y. This was due to the presence of a parent low to the east of the developing low (Fig. 8), whose northerly flow set up an MCAO with enhanced surface heat fluxes and strong baroclinicity at the leading edge of the MCAO. Or in other words, the average cyclone in X was a southbound, warm-core polar low that developed in the northerly flow of an MCAO, and the average cyclone in Y was a 'normal' baroclinic eastward moving low (Fig. 9). Strong baroclinicity, low static stability and reversed shear associated with the warm-core polar lows in X led to very strong surface winds.

Composite averages often obscure important features. The following analysis is an attempt to quantify the effects of some of the previously mentioned factors, while still retaining the extreme values for each case.

Figure 11 shows scatter plots for a selection of diagnostic parameters for X and Y at different offsets from the peak times.[4] For each variable, the 95th or 5th spatial percentiles

---

[4] As mentioned earlier, the effects of latent heat release and differential diabatic heating are complicated to assess and will not be considered here.
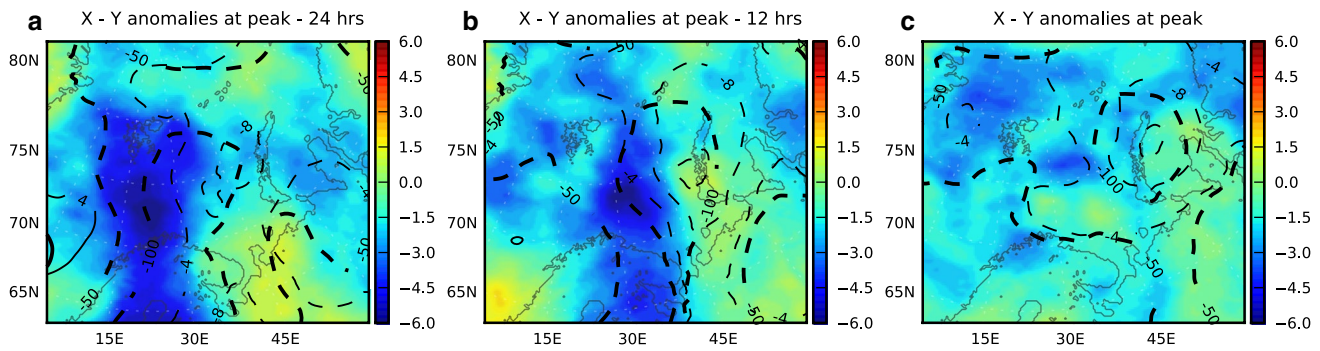
Fig. 10 The differences between the anomalies for X and the anomalies for Y. *Colours* and *contours* as in Figs. 8d–f and 9d–f
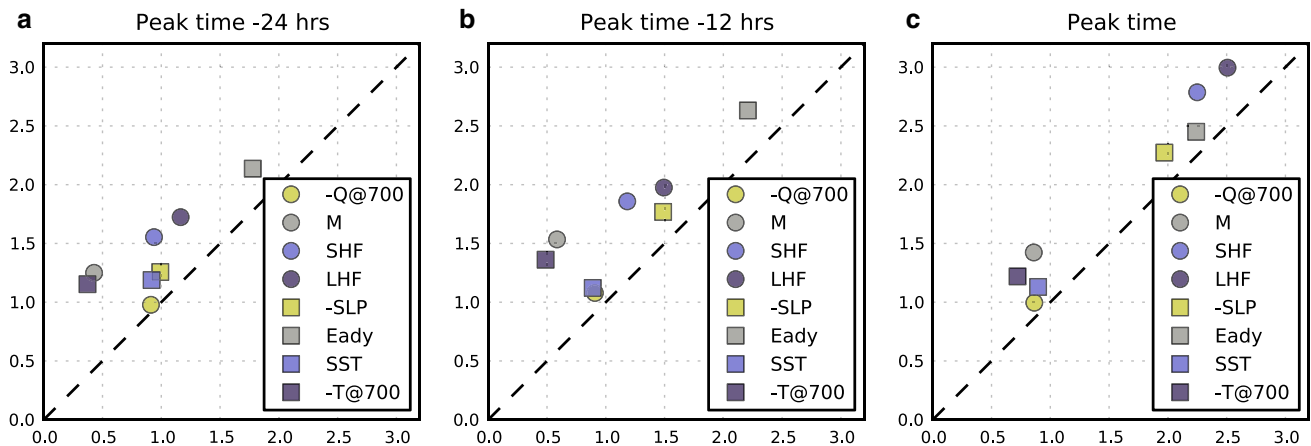

Fig. 11 The spatial 5th percentiles of normalized anomalies of SLP, 700-hPa specific humidity (Q@700) and 700-hPa temperature (T@700), and the spatial 95th percentiles of normalized anomalies of the MCAO index (M; see Eq. 5), sensible (SHF) and latent (LHF) heat flux, SST and the Eady growth rate (Eq. 4), averaged over the

cases in X (on the vertical axis) and Y (on the horizontal axis) 24 h before the peaks (**a**), 12 h before (**b**), and at the peaks (**c**). The *minus signs* in the legends mean that the values were multiplied by −1 before plotting

(depending on the variable, see figure caption for details) of normalized anomalies from climatology were computed for the same region as before and then averaged over the 12 cases in each set. No spatial averaging was involved.

An example of how to read Fig. 11 might be useful. In Fig. 11c, the marker for latent heat fluxes has a value of about 3 for X and about 2.5 for Y. This means that, on average, an area with latent heat fluxes that were 3 standard deviations above normal was found inside the study region during peak times for the cases in X (and 2.5 for Y).

At the peak times (Fig. 11c), the largest anomalies were found for sensible and latent heat fluxes, as well as for the baroclinicity (represented by the Eady growth rate). The fluxes were weaker 12 and 24 h before the peaks. The baroclinicity was also very high during the peaks and even higher 12 h before. In terms of precursor signals, the Eady growth rate was the parameter with the largest anomalies 12 and 24 h before the peaks. The remaining parameters showed weaker anomalies, but all of them still had

amplitudes of more than 1 standard deviation for X. The MCAO index M ranked highest of these, with values of around 1.5 standard deviations during the peak and 12 h before for X. The specific humidity at 700 hPa had the smallest anomalies.

In all the panels of Fig. 11, all of the anomalies are above the dashed line (i.e. they had higher values for X than for Y). It is only for the pressure that this was obvious a priori. As previously mentioned, the latent heat fluxes had anomalies of about 3 for X and 2.5 for Y at the peak times. One could say that the latent heat fluxes were about $3/2.5 = 1.2$ times more important for X than for Y. The corresponding ratios (referred to as anomaly ratios from now on) for all the variables and offset times are listed in Table 2, and will be used to assess the relative impacts (X vs. Y) of the different factors.

The MCAO index M and the temperature at 700 hPa had the largest anomaly ratios at the peak times, with values of about 1.7. One interpretation of this is that strong

Table 2 The anomaly ratios for X and Y, i.e. the average anomalies for X divided by the anomalies for Y, at the specified times relative to the peak intensity of each case

Parameter	24 h before	12 h before	At peak
SLP	1.27	1.19	1.15
MCAO index	2.92	2.62	1.66
700-hPa temperature	3.10	2.79	1.69
SST	1.29	1.26	1.26
Sensible heat flux	1.66	1.57	1.24
Latent heat flux	1.48	1.32	1.19
Eady growth rate	1.20	1.19	1.09
700-hPa specific humidity	1.07	1.19	1.15

Fig. 12 a A satellite image taken at 1232 UTC on 12 November 1990, about 2.5 h after the peak of case 2. The image was printed with the kind permission of the Dundee Satellite Receiving Station. **b** The simulated brightness temperature (*greyscale*, K) and SLP (*contours*) at 1300 UTC on the same day

wind episodes are more likely to become more extreme if these parameters have large anomalies. It is also interesting to note that the anomaly ratios for both *M* and the 700-hPa temperature were higher than 2.5 both 12 and 24 h before the peaks. This is much higher than for the other parameters. It is clearly the 700-hPa temperature fluctuations that caused the MCAO index anomalies, although (the more slowly varying) positive SST anomalies were also larger for X than for Y. The surface energy flux anomaly ratios were about 1.2 at the peaks, but these were also higher before that. The Eady growth rate anomalies were nearly equal for X and Y at the peaks (anomaly ratio of only about 1.1), but seem to have been slightly more important 12 and 24 h before (anomaly ratio of about 1.2). The specific humidity (as a possible proxy for dry intrusions) may also have played a role with anomaly ratios of nearly 1.2 at the peaks and 12 h before. The anomaly ratio for 1.27 for SLP 24 h before the peaks may reflect the importance of antecedent spin-up of the surface low (Gyakum et al. 1992).

4 Discussion

First of all, it should be noted that the hindcast was not meant to be an exact reproduction of reality. Model simulations never are, but an additional factor in this hindcast is that each individual model run had a duration of more than 1 week. Although spectral nudging was used, this is ample time for a model run to part ways with the actual weather a few days into the simulation. Case 2 (Fig. 6, second panel in the top row) is a case in point. Figure 12a shows a satellite image taken at 1232 UTC on 12 November 1990, 2.5 h after the reference time for case 2. The cyclone is clearly a polar low, and the roll clouds (Liu et al. 2004) to the west and north of the low are signs of an MCAO with reversed shear and strong surface winds. A pseudo satellite image of the simulated polar low from about the same time (Fig. 12b) makes it clear that its centre is located west
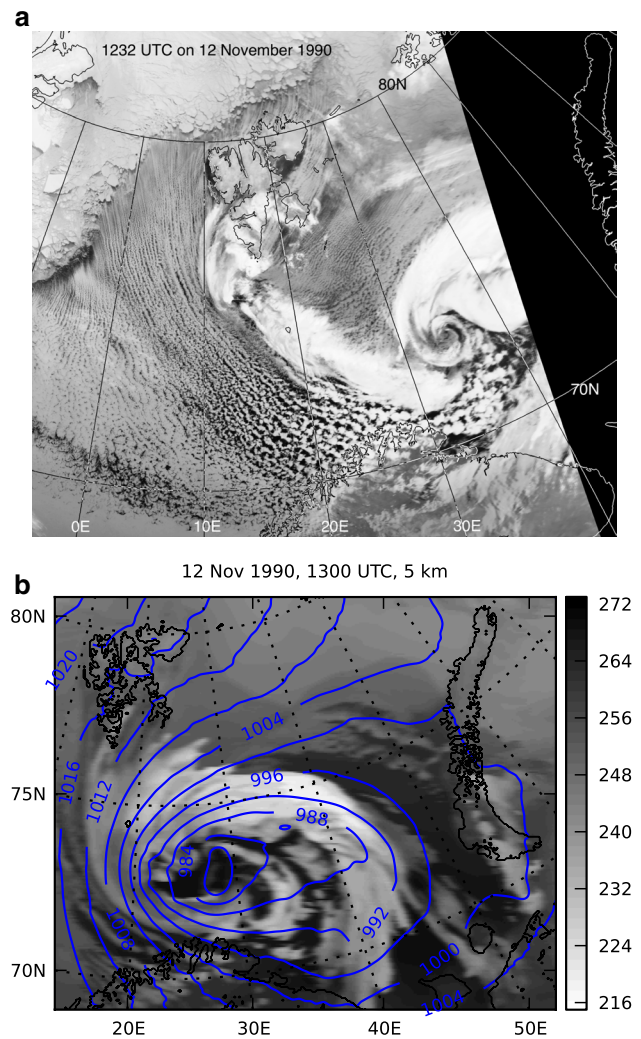
of the centre of the actual polar low. In addition, its cloud structure is not identical to the one of the actual polar low, indicating that the simulations did not succeed fully in capturing the actual development. Still, the observed weather conditions at nearby Bear Island, which has a meteorological station at at 19.00°E, 74.52°N, just north-east of the maximum wind speed in Fig. 6, were relatively severe. The maximum wind gust between 0600 and 1200 UTC on 12 November was 26.2 ms^{-1}, and the pressure dropped by 20 hPa during the 24 h before 0600 UTC on 12 November. But even though the hindcast's correlation with reality is not perfect, the evaluation section showed that the hindcast was able to span a realistic sample space for extreme winds, at least further south in the Nordic Seas region. That is a region with a much higher number of observations

feeding into the ERA-Interim than the Barents Sea region, but it is to be hoped that the ERA-Interim forcing fields are sufficiently accurate for the purposes of this study.

Polar lows in MCAOs were found to be the main cause of the most severe small-scale wind episodes over the Barents Sea. One of the reasons for this is that the 99th spatial percentile of wind speed was used to identify the episodes. Why did I use that particular percentile? The entire region that was scanned for events covers an area of 680,000 km^2, so the spatial 99th percentile at any given time represents a value that is exceeded by an area of 6,800 km^2, or a square with 82 km on each side. I also tried to use the spatial 95th percentile (equivalent to a square with sides of 185 km), but this yielded a very similar set of cases. For instance: the first seven cases in that time series were also among the 12 cases in X. For the spatial 90th percentile (corresponding to a square with 261 km on each side), the first five cases were also found in X, but then some of the remaining cases were on synoptic scales. It would have been interesting to include a composite analysis of the most intense cases for the spatial 90th percentile, but this was avoided in the interest of maintaining a clear focus on small-scale features.

An interesting question that arises when looking at the cases in Fig. 6 is: *Why do the most extreme cases tend to occur in the western part of the Barents Sea?* The most obvious reason is that the extreme cases always occur in MCAOs with northerly flow. The mean winter wind direction over the western part of the Barents Sea is northerly, while the eastern part is dominated by southerly winds (see Fig. 2 in Kolstad 2008). This is at least partly because cyclones tend to be stuck against the eastern barrier that is Novaya Zemlya. Also, the strongest winds in a cyclone are usually found where the local winds associated with the cyclone coincide with the background flow, i.e. to the south-west of the low if the flow is from the north-west. Another reason for the geographical differences is that the mesocyclones that cause the strong winds are fuelled by warm advection in combination with MCAOs. The western part of the Barents Sea has easier access to warm air from the Norwegian Sea. In addition, the sea surface is cooler further east in the Barents Sea (Korablev et al. 2014), yielding weaker MCAO index values (and weaker surface heat fluxes) than in the western part. Still, some of the cases in Fig. 6 did occur in the east. Cases 1 and 4 came to pass as warm occlusions in synoptic cyclones moved south and intensified as they connected with fast-moving upper-levels cut-off lows that appeared over the Barents Sea. Case 8 was more similar to case 2, but occurred so far east because it hooked up with an existing mesoscale low that was located there. The warm air masses that were needed for the all three developments originated over the Norwegian Sea, but they had been transported eastwards by synoptic-scale features.

At least two previous studies (Kolstad and Bracegirdle 2008; Zahn and von Storch 2010) have indicated a future decrease in polar low activity in the north-east Atlantic region. The main reason is a projected increase in air temperatures, and the present study confirms that low air temperatures and polar lows are major factors in the development of strong wind episodes. As such, the results presented here indirectly imply that the frequency and strength of extreme winds in the Barents Sea region may decrease if the warming of the lower Arctic air masses (e.g., Bekryaev et al. 2010) continues.

In quantitative terms, the parameters that displayed the largest anomalies during strong wind episodes were the surface heat fluxes and the Eady growth rate (i.e. the baroclinicity) at low levels. Low static stability (i.e. high values of the MCAO index) due to MCAOs over relatively warm water seemed to be less important, but the anomalies for the MCAO index and the air temperature at 700 hPa were much larger for X than for Y. This suggests that MCAOs can be a catalyst for really extreme winds in environments that are already conducive to strong winds. This makes sense for a number of reasons:

1. Polar lows in MCAOs often develop warm cores (e.g., Shapiro et al. 1987; Emanuel and Rotunno 1989; Føre et al. 2011). Along the interface between the warm core and the cold air masses in the MCAO to the west and south-west of it, the baroclinicity is high and the thermal wind is antiparallel to the actual wind (reversed shear), and this can lead to strong near-surface winds (Kolstad 2006).
2. Over an MCAO the tropopause is lowered, and this facilitates dry intrusions from the lower stratosphere, which again may help to spin up polar lows (Grønås and Kvamstø 1995) and other marine cyclones (Browning 1997).
3. Low static stability makes it possible for high-momentum air to penetrate down towards the surface (Schultz and Sienkiewicz 2013; Baker et al. 2014).

The higher MCAO index values for X than for Y imply that if the ocean surface is slightly warmer than usual and particularly cold (and dry) air breaks out from the north, a strong cyclone can turn into an explosive one. A similar result was obtained by Gyakum and Danielson (2000) in their composite analysis of explosive cyclones over the western North Pacific.

As mentioned earlier, observational data is sparse in the Barents Sea region and elsewhere in the Arctic, so forecasters are often in need of simple indicators when evaluating the potential for strong winds. In fact, the polar low forecasters in Tromsø, Norway monitor the difference between the SST and the temperature at 500 hPa (Gunnar Noer,

personal communication). The results presented here indicate that that particular parameter and related ones[5] are highly pertinent. Already 24 h before the storms' peak intensity, the MCAO index M was higher than normal, acting as a possible harbinger of extreme winds for experienced forecasters. As the quality and resolution of the forecast models increase with time, it is in data-sparse regions that human experience still gives a vital edge.

References

Årthun M, Eldevik T, Smedsrud LH, Skagseth Ø, Ingvaldsen R (2012) Quantifying the influence of Atlantic heat on Barents sea ice variability and retreat. J Clim 25(13):4736–4743

Bader J, Mesquita MD, Hodges KI, Keenlyside N, Østerhus S, Miles M (2011) A review on Northern Hemisphere sea-ice, storminess and the North Atlantic Oscillation: observations and projected changes. Atmos Res 101(4):809–834

Baker LH, Gray SL, Clark PA (2014) Idealised simulations of sting-jet cyclones. Q J R Meteorol Soc 140(678):96–110. doi:10.1002/qj.2131

Bekryaev RV, Polyakov IV, Alexeev VA (2010) Role of polar amplification in long-term surface air temperature variations and modern Arctic warming. J Clim 23(14):3888–3906

Bracegirdle TJ, Gray SL (2008) An objective climatology of the dynamical forcing of polar lows in the Nordic Seas. Int J Climatol 28(14):1903–1919

Browning K (1997) The dry intrusion perspective of extra-tropical cyclone development. Meteorol Appl 4(04):317–324

Browning KA (2004) The sting at the end of the tail: damaging winds associated with extratropical cyclones. Q J R Meteorol Soc 130(597):375–399. doi:10.1256/qj.02.143

Chen F, Dudhia J (2001) Coupling an advanced land surface–hydrology model with the Penn State–NCAR MM5 modeling system. Part I: model implementation and sensitivity. Mon Weather Rev 129:569–585

Cleveland WS, Devlin SJ (1989) Locally weighted regression: an approach to regression analysis by local fitting. J Am Stat Assoc 83:596–610

Courant R, Friedrichs K, Lewy H (1928) Über die partiellen Differenzengleichungen der mathematischen Physik. Matematische Annalen 100:32–37

Dacre HF, Gray SL (2009) The spatial distribution and evolution characteristics of North Atlantic cyclones. Mon Weather Rev 137(1):99–115

Dee DP et al (2011) The ERA-Interim reanalysis: configuration and performance of the data assimilation system. Q J R Meteorol Soc 656:553–597

Duncan CN (1978) Baroclinic instability in a reversed shear flow. Meteorol Mag 107:17–23

Emanuel KA, Rotunno R (1989) Polar lows as arctic hurricanes. Tellus 41A(1):1–17

Føre I, Kristjánsson JE, Saetra Ø, Breivik Ø, Røsting B, Shapiro M (2011) The full life cycle of a polar low over the Norwegian Sea observed by three research aircraft flights. Q J R Meteorol Soc 137(660):1659–1673

Føre I, Kristjánsson JE, Kolstad EW, Bracegirdle TJ, Saetra Ø, Røsting B (2012) A hurricane-like polar low fuelled by sensible heat flux: high-resolution numerical simulations. Q J R Meteorol Soc 138(666):1308–1324. doi:10.1002/qj.1876

Gautier DL, Bird KJ, Charpentier RR, Grantz A, Houseknecht DW, Klett TR, Moore TE, Pitman JK, Schenk CJ, Schuenemeyer JH et al (2009) Assessment of undiscovered oil and gas in the Arctic. Science 324(5931):1175–1179

Grønås S (1995) The seclusion intensification of the new year's day storm 1992. Tellus 47A(5):733–746. doi:10.1034/j.1600-0870.1995.00116.x

Grønås S, Kvamstø NG (1995) Numerical simulations of the synoptic conditions and development of Arctic outbreak polar lows. Tellus 47A(5):797–814. doi:10.1034/j.1600-0870.1995.00121.x

Gyakum JR, Danielson RE (2000) Analysis of meteorological precursors to ordinary and explosive cyclogenesis in the western North Pacific. Mon Weather Rev 128(3):851–863

Gyakum JR, Roebber PJ, Bullock TA (1992) The role of antecedent surface vorticity development as a conditioning process in explosive cyclone intensification. Mon Weather Rev 120(8):1465–1489

Hoffman RN, Leidner SM (2005) An introduction to the near-real-time QuikSCAT data. Weather Forecast 20(4):476–493

Holton JR (2004) An introduction to dynamic meteorology, 4th edn. Academic Press, Massachusetts

Hoskins BJ, Hodges KI (2002) New perspectives on the Northern Hemisphere winter storm tracks. J Atmos Sci 59(6):1041–1061

Hoskins BJ, Valdes PJ (1990) On the existence of storm-tracks. J Atmos Sci 47(15):1854–1864

Iacono MJ et al (2008) Radiative forcing by long-lived greenhouse gases: calculations with the AER radiative transfer models. J Geophys Res 113(D13):103. doi:10.1029/2008JD009944

Janjic ZI (1994) The step-mountain eta coordinate model: further developments of the convection, viscous sublayer and turbulence closure schemes. Mon Weather Rev 122:927–945

Kain JS (2004) The Kain–Fritsch convective parameterization: an update. J Appl Meteorol 43(1):170–181

Kolstad EW (2006) A new climatology of favourable conditions for reverse-shear polar lows. Tellus 58A:344–354

Kolstad EW (2008) A QuikSCAT climatology of ocean surface winds in the Nordic Seas: identification of features and comparison with the NCEP/NCAR reanalysis. J Geophys Res 113(D11):106

Kolstad EW, Bracegirdle TJ (2008) Marine cold-air outbreaks in the future: an assessment of IPCC AR4 model results for the Northern Hemisphere. Clim Dyn 30(7–8):871–885

Korablev A, Smirnov A, Baranova OK (2014) Climatological atlas of the Nordic Seas and northern North Atlantic. In: Seidov D, Parsons AR (eds) NOAA Atlas NESDIS 77

Lindzen R, Farrell B (1980) A simple approximate result for the maximum growth rate of baroclinic instabilities. J Atmos Sci 37(7):1648–1654

Liu AQ, Moore GWK, Tsuboki K, Renfrew IA (2004) A high-resolution simulation of convective roll clouds during a cold-air outbreak. Geophys Res Lett 31:L03101. doi:10.1029/2003GL018530

McInnes H, Kristiansen J, Kristjánsson JE, Schyberg H (2011) The role of horizontal resolution for polar low simulations. Q J R Meteorol Soc 137(660):1674–1687

Montgomery MT, Farrell BF (1992) Polar low dynamics. J Atmos Sci 49(24):2484–2505

Moore G (2013) The Novaya Zemlya bora and its impact on Barents Sea air–sea interaction. Geophys Res Lett 40(13):3462–3467

Moore GWK, Renfrew IA, Pickart RS (2012) Spatial distribution of air–sea heat fluxes over the sub-polar North Atlantic Ocean. Geophys Res Lett 39:L18806. doi:10.1029/2012GL053097

Noer G, Saetra Ø, Lien T, Gusdal Y (2011) A climatological study of polar lows in the Nordic Seas. Q J R Meteorol Soc 137(660):1762–1772

---

[5] Here, as in Bracegirdle and Gray (2008), the level at 700 hPa gave better results than the one at 500 hPa, probably because most of the systems are shallow.

Nordeng TE, Rasmussen EA (1992) A most beautiful polar low: a case study of a polar low development in the Bear Island region. Tellus 44A(2):81–99

Petterssen S (1935) Contribution to the theory of frontogenesis. Geofys Publ XI(6):5–27

Rasmussen E (1985) A case study of a polar low development over the Barents Sea. Tellus 37A(5):407–418

Rasmussen EA, Turner J (eds) (2003) Polar lows. Cambridge University Press, Cambridge

Reeve MA, Kolstad EW (2011) The Spitsbergen south cape tip jet. Q J R Meteorol Soc 137(660):1739–1748

Renfrew IA, Moore G, Clerk AA (1997) Binary interactions between polar lows. Tellus 49A(5):577–594

Roebber PJ, Schumann MR (2011) Physical processes governing the rapid deepening tail of maritime cyclogenesis. Mon Weather Rev 139(9):2776–2789

Schultz DM, Sienkiewicz JM (2013) Using frontogenesis to identify sting jets in extratropical cyclones. Weather Forecast 28(3):603–613

Shapiro MA, Keyser DA (1990) Fronts, jet streams, and the tropopause. In: Newton CW, Holopainen EO (eds) Extratropical cyclones: the Erik Palmen memorial volume. American Meteorological Society, pp 167–191

Shapiro MA, Fedor LS, Hampel T (1987) Research aircraft measurements of a polar low over the Norwegian Sea. Tellus 39A(4):272–306. doi:10.1111/j.1600-0870.1987.tb00309.x

Skamarock WC et al (2008) A description of the advanced research WRF version 3. Technical Report. National Center for Atmospheric Research, Colorado

Stroeve JC et al (2012) Trends in Arctic sea ice extent from CMIP5, CMIP3 and observations. Geophys Res Lett 39(16)

Thompson G, Field PR, Rasmussen RM, Hall WD (2008) Explicit forecasts of winter precipitation using an improved bulk microphysics scheme. Part II: implementation of a new snow parameterization. Mon Weather Rev 136:5095–5115

Wang CC, Rogers JC (2001) A composite study of explosive cyclogenesis in different sectors of the North Atlantic. Part I: cyclone structure and evolution. Mon Weather Rev 129(6):1481–1499

Zahn M, von Storch H (2008) A long-term climatology of North Atlantic polar lows. Geophys Res Lett 35:L22702. doi:10.1029/2008GL035769

Zahn M, von Storch H (2010) Decreased frequency of North Atlantic polar lows associated with future climate warming. Nature 467(7313):309–312